Similarity scaling of turbulence spectra and cospectra in a shallow tidal flow

Ryan K. Walter,[1] Nicholas J. Nidzieko,[2,3] and Stephen G. Monismith[1]

Received 18 March 2011; revised 8 July 2011; accepted 25 July 2011; published 15 October 2011.

[1] Measured turbulence power spectra, cospectra, and ogive curves from a shallow tidal flow were scaled using Monin-Obukhov similarity theory to test the applicability to a generic tidal flow of universal curves found from a uniform, neutrally stable atmospheric boundary layer (ABL). While curves from individual 10 min data bursts deviate significantly from similarity theory, averages over large numbers of sufficiently energetic bursts follow the general shape. However, there are several differences: (1) Variance in the measured curves was shifted toward higher frequencies, (2) at low frequencies, velocity spectra were significantly more energetic than theory while cospectra were weaker, and (3) spectral ratios of momentum flux normalized by turbulent kinetic energy (TKE) indicate decreased fluxes and/or elevated TKE levels. Several features of the turbulence structure may explain these differences. First, turbulent dissipation exceeded production, indicating nonequilibrium turbulence, possibly from advection of TKE. Indeed, using the production rate rather than dissipation markedly improves agreement in the inertial subrange. Second, spectral lag of the largest eddies due to inhomogeneous boundary conditions and decaying turbulence could explain spectral deviations from theory at low frequencies. Finally, since the largest eddies dominate momentum transfer, the consequence of the cospectra difference is that calculated ogive curves produced smaller total momentum fluxes compared to theory, partly because of countergradient fluxes. While ABL similarity scaling applied to marine bottom boundary layers (MBBLs) will produce curves with the general shape of the universal curves, care should be taken in determining details of turbulent energy and stress estimates, particularly in shallow and inhomogeneous MBBLs.

Citation: Walter, R. K., N. J. Nidzieko, and S. G. Monismith (2011), Similarity scaling of turbulence spectra and cospectra in a shallow tidal flow, *J. Geophys. Res.*, *116*, C10019, doi:10.1029/2011JC007144.

1. Introduction

[2] Turbulence power spectra of the along-channel (u') and vertical (w') velocity fluctuations are often used to describe the range of scales in turbulence, in particular the dominant eddy sizes responsible for turbulent transfer as well as the distribution of variance with frequency [*Roth et al.*, 1989]. Likewise, turbulence cospectra, or their integral versions, ogive curves, are used to describe the distribution of the covariance ($u'w'$) across the frequency domain, where $u'w'$ represents a vertical flux of along-channel momentum that is due to turbulent fluctuations.

[3] Monin-Obukhov similarity theory postulates that in a uniform, homogeneous atmospheric boundary layer (ABL), turbulence spectra, cospectra, and ogive curves will take universal forms when appropriately nondimensionalized. In particular, for the neutrally stable case, one in which turbulent production is dominated by mechanical shear with negligible production by buoyancy, only three parameters are needed to collapse the curves to a universal form: the friction velocity (u_*), the average horizontal velocity magnitude (U_{hor}), and the height above the surface (z). Using Monin-Obukhov theory and data acquired in a flat, uniform ABL in Kansas, *Kaimal et al.* [1972] derived a set of nondimensional curves for the power spectra of along-channel velocity fluctuations ($S^*_{u'u'}$), power spectra of the vertical velocity fluctuations ($S^*_{w'w'}$), and cospectra of along-channel and vertical velocity fluctuations ($Co^*_{u'w'}$):

$$S^*_{u'u'}(f^*) = \frac{S_{u'u'}(f)\cdot U_{\mathrm{hor}}}{z\cdot u_*^2} = \frac{105}{\left(1+33\cdot f^*\right)^{5/3}}, \quad (1)$$

$$S^*_{w'w'}(f^*) = \frac{S_{w'w'}(f)\cdot U_{\mathrm{hor}}}{z\cdot u_*^2} = \frac{2}{\left[1+5.3\cdot\left(f^*\right)^{5/3}\right]}, \quad (2)$$

$$Co^*_{u'w}(f^*) = \frac{-Co_{u'w'}(f)\cdot U_{\mathrm{hor}}}{z\cdot u_*^2} = \frac{14}{\left(1+9.6\cdot f^*\right)^{2.4}}, \quad (3)$$

[1] Environmental Fluid Mechanics Laboratory, Stanford University, Stanford, California, USA.
[2] Applied Ocean Physics and Engineering, Woods Hole Oceanographic Institution, Woods Hole, Massachusetts, USA.
[3] Now at Horn Point Laboratory, University of Maryland Center for Environmental Science, Cambridge, Maryland, USA.

0148-0227/11/2011JC007144

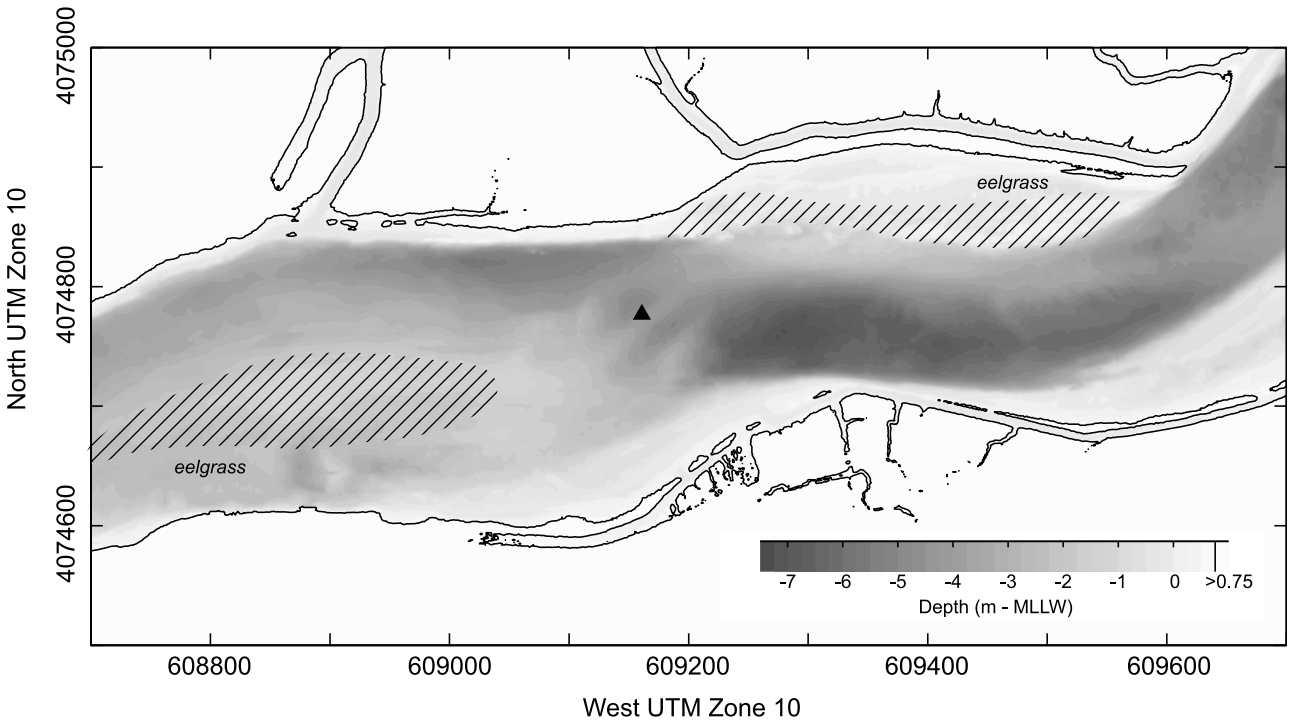

Figure 1. The experimental site showing the main channel of Elkhorn Slough, CA, with the ocean located about 1 km west of the study site. The location of the colocated ADV and ADCP is indicated with a black triangle. Depths are in meters below mean lower low water, and white shading depicts land greater than 0.75 m elevation. Black dashed lines indicate the approximate extent of eelgrass coverage obtained from aerial photos. Figure modified from *Nidzieko et al.* [2006], © American Meteorological Society. Reprinted with permission.

where a superscript asterisk represents a nondimensional quantity, f is the frequency, and $f^* = fz/U_{\mathrm{hor}}$ is a nondimensional frequency [*Kaimal et al.*, 1972]. The above empirical relationships were derived assuming that equilibrium turbulence exists, whereby production (P) of turbulent kinetic energy (k) is in balance with dissipation (ε) of turbulent kinetic energy.

[4] Given this, measured spectra, cospectra, and ogive curves, when made nondimensional appropriately, are generally supposed to exhibit the relations found by *Kaimal et al.* [1972], hereafter referred to as the Kaimal curves [see, e.g., *Kristensen and Fitzjarrald*, 1984; *Roth et al.*, 1989; *Al-Jiboori et al.*, 2001]. Since then, numerous studies performed in marine bottom boundary layers (MBBLs), such as those found in coastal and/or estuarine environments, have used Kaimal curves derived from the ABL for calculating nondimensional turbulence spectra, cospectra, and ogive curves [e.g., *Soulsby*, 1977; *Feddersen and Williams*, 2007]. Various investigators have used the Kaimal curves in the MBBLs for various purposes including filtering waves from turbulence [*Shaw and Trowbridge*, 2001; *Feddersen and Williams*, 2007; *Kirincich et al.*, 2010], comparing the general shape and form to the Kaimal curves [*Soulsby*, 1977; *Scully et al.*, 2011], analyzing the vertical structure of Reynolds stresses [*Feddersen and Williams*, 2007], determining turbulent scales in the coastal ocean [*Trowbridge and Elgar*, 2003], and modeling vorticity flux spectra [*Lien and Sanford*, 2000]. In all of these cases, however, the Kaimal scaling was assumed to hold. Here, instead, we test the validity of the Kaimal scaling using data acquired in a fairly generic estuarine tidal flow. Turbulence spectra, cospectra, and ogive curves of a well-mixed, tidal flow will be scaled according to Monin-Obukhov similarity theory and compared to the Kaimal curves.

2. Site Description and Methods

2.1. Experimental Setup

[5] Velocity data were collected over a spring-neap cycle from 12 to 28 October 2004 in the main channel of Elkhorn Slough, California, located in the center of Monterey Bay (Figure 1). Elkhorn Slough is a shallow, tidally forced estuary that is protected from significant surface wave activity. The site is characterized by a maximum tidal range of ~2.5 m [*Nidzieko et al.*, 2006]. The bed in the main channel is a mix of mud and shell hash, with several intermittent patches of eel grass and deep scour holes. Vertical density data in the main channel of Elkhorn Slough were obtained from the Land/Ocean Biogeochemical Observatory (LOBO), which is part of the Monterey Bay Aquarium Research Institute (MBARI). The observations (not shown) depict approximately well-mixed conditions throughout the study period, except around 21 October, where precipitation occurred and caused small density differences between surface waters and deeper waters. However, most events during this precipitation event did not fit

the data quality criteria (likely because it was the first precipitation event of the season) and were discarded ($\overline{\Delta\rho} \approx 1.5 \times 10^{-2}$ kg/m^3 for time periods analyzed excluding the bracketed region around events that were discarded because of the precipitation event, where $\overline{\Delta\rho}$ is the average density difference between measurements made at 2 m depth and the surface). Furthermore, including or excluding this small period of weak stratification did not affect any of the major results and/or conclusions of this paper (see section 4.1).

[6] Instantaneous velocity measurements were made in the main channel at a height of 1 m above the bottom using a Nortek 6-MHz Vector acoustic Doppler velocimeter (ADV). Samples were collected in 10 min bursts, every half hour, at a sampling frequency of 16 Hz, capturing both the spring and neap events over the 16 day sampling period. Colocated with the ADV was a Teledyne-RDI 1.2-MHz Workhorse acoustic Doppler current profiler (ADCP). The ADCP was deployed in mode 12, sampling 16 subpings at 40 ms intervals for an actual recording rate of 1 Hz [*Nidzieko et al.*, 2006]. The ADCP was programmed with 0.25 m bins, with the location of the center of the bin at 1 m coincident with the ADV sample volume. Both the ADV and ADCP were leveled by divers in order to minimize instrument tilt errors. A more detailed description of the experimental setup can be found in the paper by *Nidzieko et al.* [2006].

2.2. Data Analysis

2.2.1. Data Processing

[7] We computed cospectra and spectra for all data bursts including all tidal phases. However, it was clear that near slack water ($|U| < 0.1$ m/s), the computed curves were too noisy to usefully examine turbulence behavior. On the other hand, outside this velocity range and for all tidal phases, shapes and variations in the shape of spectra and cospectra appeared similar. Hence, we focused on maximum flood and ebb currents in further analysis, since these present the clearest picture of the behavior of the turbulence field (ADV velocity range in m/s of $0.32 \le |U| \le 0.55$ and $0.30 \le |U| \le 0.73$ for the max flood and ebb currents, respectively). Velocity measurements for both the ADV and ADCP were converted into along-channel (u), cross-channel (v), and vertical (w) velocities, using a principal-axes analysis [*Emery and Thomson*, 2004]. The ADV and ADCP had very similar flow orientations so the same angle of rotation was used for both. Positive u velocities were defined as up-estuary, with v and w defined as across-channel and vertical, respectively. Average (U, V, W) and fluctuating (u', v', w') velocities were computed using 10 min windows, an average that represents a trade-off between capturing desired turbulent length scales and maintaining quasi-stationary statistics [*Soulsby*, 1980]. ADV data with correlations less than 0.85 and $u' > +/-0.35$ m s^{-1} were discarded and linearly interpolated back into the data set. Ten minute windows with more than 5% discarded data were not used for further analyses.

2.2.2. Spectral Calculations

[8] Power spectra of the along-channel and vertical ADV velocities were calculated using the fluctuating components (u' and w'), while cross spectra were calculated for the vertical covariance terms ($u'w'$ and $v'w'$), both using the fast Fourier technique over 10 min windows. Each 10 min window (n = 9600) was linearly detrended and then split into four smaller segments (n = 2400), which were zero padded to achieve the next power of 2 for the fast Fourier transform and to increase frequency resolution (n = 4096). The choice of segment length represented a compromise between the increased number of degrees of freedom (DOFs), decreased frequency resolution, and the ability to delineate the low-frequency end of the spectrum [*Emery and Thomson*, 2004]. A Hamming window with 50% overlap was applied to each segment in order to reduce spectral leakage, spectral densities were calculated using the fast Fourier technique, and segments were block averaged to smooth the spectra and cross spectra [*Emery and Thomson*, 2004]. Thus, each 10 min window had spectral values (n = 2049) up to the Nyquist frequency with a frequency resolution of $\Delta f = 3.9 \times 10^{-3}$ Hz. The "equivalent" number of DOFs ($\nu = 23.6$) was determined by taking into account the type of window, percentage of overlap, and the size of the segments, and 95% confidence intervals were calculated using a chi-square variable analysis [*Emery and Thomson*, 2004]. The confidence limits for individual spectra indicate that the ratio of true spectrum to the measured spectrum at a particular frequency will be about 0.6 and 1.9 for the lower and upper 95% confidence limits, respectively [*Emery and Thomson*, 2004]. As is commonly done, ogive curves ($Og_{u'w'}$) were calculated by taking the cumulative integral of the cospectra, the real parts of the cross spectra, and nondimensionalized as,

$$Og_{u'w'}\left(f^*\right) = \frac{-\int_0^f Co_{u'w'}\left(\tilde{f}\right)d\tilde{f}}{u_*^2}. \tag{4}$$

[9] After this, the spectra, cospectra, ogive curves, and frequency components were all made nondimensional according to equations (1)–(4). The average horizontal speed was calculated as $U_{\mathrm{hor}} = \sqrt{U^2 + V^2}$ using the ADV data, with V usually 1 to 2 orders of magnitude smaller than U, hence contributing negligibly to U_{hor}. The friction velocity squared is defined as $u_*^2 = \tau/\rho$, where τ is the bottom shear stress and ρ is the density. Friction velocities can be estimated by fitting mean velocity profiles to a logarithmic profile, directly using Reynolds stress measurements near the bed, or with measurements of dissipation of turbulent kinetic energy and the assumption of equilibrium turbulence [e.g., *Sanford and Lien*, 1999]. The dissipation method is not valid in this study since equilibrium turbulence is not present (section 4.3). Likewise, previous studies in ocean and estuarine boundary layers have found deviations from a simple logarithmic dependence and the existence of multiple log layers [*Perlin et al.*, 2005; *Sanford and Lien*, 1999]. Studies in the ABL commonly estimate bed stress at the particular measurement height, assuming a constant-stress layer over the ABL [e.g., *McNaughton and Laubach*, 2000; *Smeets et al.*, 1998; *Zhang et al.*, 2010], an assumption generally not valid over the entire MBBL. *Kaimal et al.* [1972] used a drag plate to estimate friction velocities in the ABL and found that stresses were constant with height to within 20% of the surface stress [*Haugen et al.*, 1971]. In this study, vertical profiles of Reynolds stresses estimated from the ADCP indicate a small region of nearly constant stress in the bottom 1.5 m. Thus, we

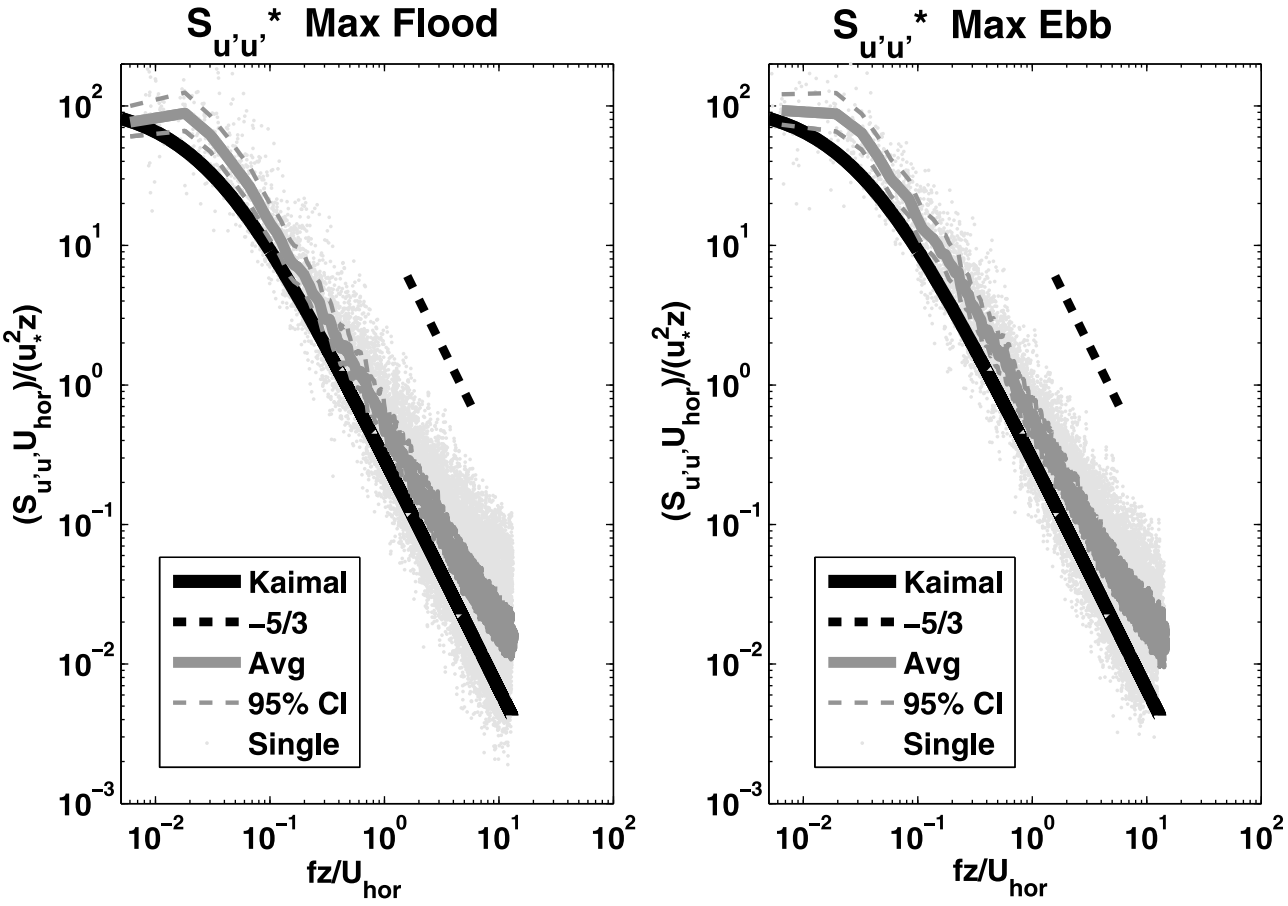

Figure 2. Nondimensional power spectra of along-channel velocity fluctuations for the max (left) flood and (right) ebb events. The individual spectra are denoted by light gray dots, the frequency-averaged spectrum by a solid dark gray line, 95% confidence intervals for the frequency averaged spectrum by dashed gray lines, the *Kaimal et al.* [1972] universal curve by a solid black line, and the −5/3 power law in the inertial subrange by a dashed black line.

will approximate the friction velocity using the average vertical Reynolds stresses near the bed as

$$u_*^2 = -\sqrt{\left(-\overline{u'w'}\right)^2 + \left(-\overline{v'w'}\right)^2}, \tag{5}$$

where an overbar represents a 10 min average and the stresses are measured with the ADV at a height of 1 m above the bottom. However, the cross-channel, vertical Reynolds stress $\left(-\overline{v'w'}\right)$ was consistently 1 to 2 orders of magnitude smaller than the along-channel, vertical Reynolds stress $\left(-\overline{u'w'}\right)$, which makes $\left(-\overline{v'w'}\right)^2$ negligible in the squared friction velocity calculation. Given this, the squared friction velocity was estimated by integrating the $Co_{u'w'}$ determined from the ADV data over a 10 min window:

$$u_*^2 = -\int_0^\infty Co_{u'w'}(f)df. \tag{6}$$

For spectral calculations of the max ebb events, u and v velocities were rotated 180° or multiplied by −1 so that normalized cospectra and ogive curves would yield positive values.

[10] Finally, the nondimensional curves were all averaged together in frequency space over all max flood and ebb events, respectively. The same number of spectrally calculated frequency bins (n = 2049) was used in calculating the nondimensional frequency bins. In order to capture all events in the nondimensional frequency range, the maximum nondimensional frequency range of all individual events was selected and split into n = 2049 nondimensional frequency bins ($\Delta f^* = 1.2 \times 10^{-2}$). After this, all nondimensional curves ($\overline{n}$ = 50 for flood and $\overline{n}$ = 42 for ebb) within a particular nondimensional frequency bin were ensemble averaged together to create the nondimensional frequency-averaged curves. Frequency-averaged 95% confidence intervals were calculated similarly to individual 10 min spectra using a chi-square variable analysis, but with an increased number of DOFs, depending on the number of spectra averaged in a particular nondimensional frequency bin [*Emery and Thomson*, 2004]. All nondimensional curves were plotted up to $f^* \approx 14$, where noise begins to dominate the signal, and averaged nondimensional cospectra were smoothed

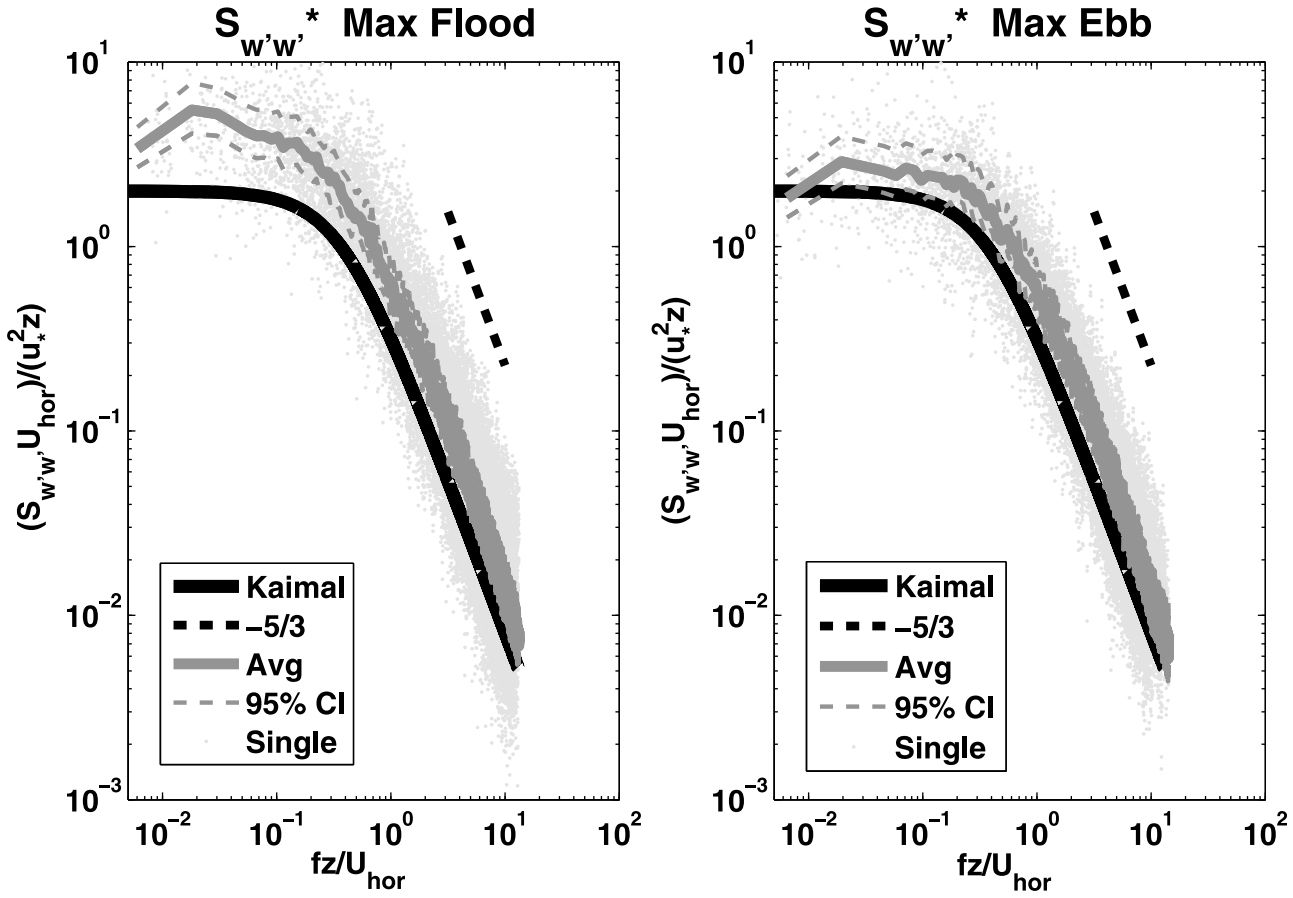

Figure 3. Nondimensional power spectra of vertical velocity fluctuations for the max (left) flood and (right) ebb events. The individual spectra are denoted by light gray dots, the frequency- averaged spectrum by a solid dark gray line, 95% confidence intervals for the frequency averaged spectrum by dashed gray lines, the *Kaimal et al.* [1972] universal curve by a solid black line, and the −5/3 power law in the inertial subrange by a dashed black line.

at high frequencies ($f^* > 6$) using a moving average in f^* over 50 points, which comprises less than 2.5% of the entire record. This plotting range and smoothing does not affect any of the conclusions or analysis of this paper.

2.2.3. Turbulent Production and Dissipation

[11] The turbulent kinetic energy (TKE) is defined as [*Pope*, 2000]

$$k = \frac{1}{2}\left[\overline{(u')^2} + \overline{(v')^2} + \overline{(w')^2}\right]. \tag{7}$$

In equilibrium, unstratified, homogeneous sheared turbulent flows [*Pope*, 2000], it is generally found that production of TKE by shear is balanced by its dissipation by small-scale strains. Thus, the extent to which this holds is often a measure of the extent to which a given shear flow resembles a canonical homogeneous shear.

[12] The shear production (P) of TKE is given by

$$P = -\overline{u'w'}\frac{\partial U}{\partial z} - \overline{v'w'}\frac{\partial V}{\partial z}. \tag{8}$$

In our case, the Reynolds stresses are measured directly from the ADV and vertical velocity gradients are calculated using the ADCP.

[13] In contrast, dissipation of turbulent kinetic energy (ε) was estimated using spectra of the vertical velocity fluctuations assuming Taylor's frozen field turbulence hypothesis holds and using Kolmogorov's famous −5/3 law [e.g., *Shaw et al.*, 2001],

$$S_{w'w'}(f) = \frac{12}{55}\alpha\varepsilon^{2/3}\left(\frac{U}{2\pi}\right)^{2/3} f^{-5/3}, \tag{9}$$

where $\alpha = 1.56$ is the empirical Kolmogorov constant for velocity. The spectrum of vertical velocity fluctuations was used since this velocity component is the least noisy [*Voulgaris and Trowbridge*, 1998]. Dissipation was estimated by fitting a power law in the inertial subrange using several hundred points between frequencies of 1 and 2.5 Hz, encompassing the range where the inertial subrange exists in our data. Power law fits to the spectra in the inertial subrange had mean exponent values of −1.65 and −1.67 for all flood and ebb events, respectively, and never deviated significantly from −5/3, indicating the existence of an inertial

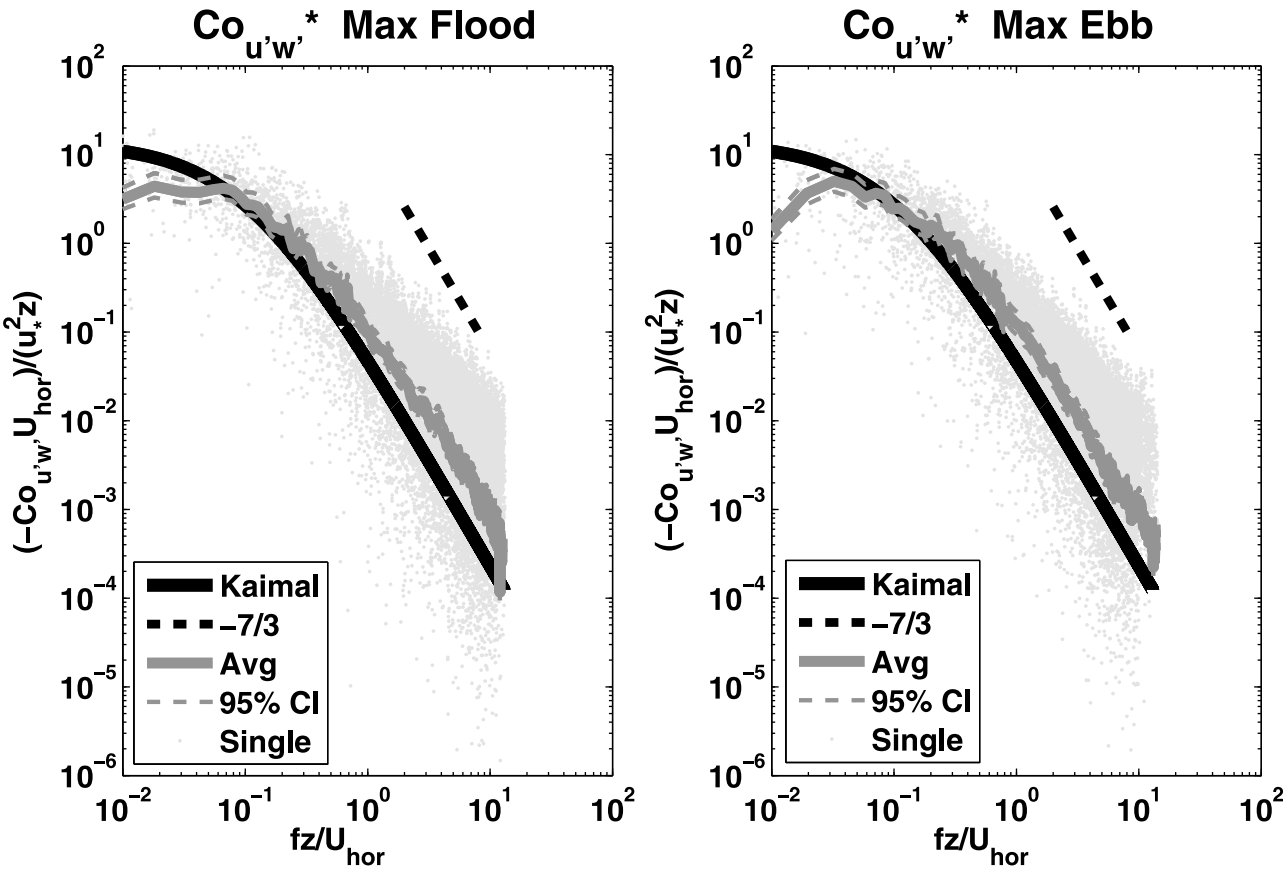

Figure 4. Nondimensional cospectra of along-channel and vertical velocity fluctuations for the max (left) flood and (right) ebb events. The individual cospectra are denoted by light gray dots, the frequency-averaged cospectrum by a solid dark gray line, 95% confidence intervals for the frequency-averaged cospectrum by dashed gray lines, the *Kaimal et al.* [1972] universal curve by a solid black line, and the −7/3 power law in the inertial subrange by a dashed black line.

subrange and adequate separation between the production and dissipation length scales [cf., *Gross and Nowell*, 1985]. Equation (9) was used to calculate dissipation by choosing values of $S_{w'w'}$ and f in the inertial subrange and subtracting off the ADV noise floor from $S_{w'w'}$.

3. Results

3.1. Velocity Power Spectra

[14] Individual and ensemble averaged, nondimensional power spectra of the along-channel velocity fluctuations are seen in Figure 2 for both the max flood and ebb events. They are plotted against the Kaimal curves and the −5/3 power law in the inertial subrange predicted by turbulent theory [*Pope*, 2000].

[15] While individual 10 min data bursts are scattered and often deviate significantly from similarity theory, the average spectra for both events follow the general trend and slope of the Kaimal curves and −5/3 power law, particularly in the inertial subrange. However, the calculated averages are shifted to the right of the Kaimal curves, indicating more energy at a given frequency compared to the Kaimal spectrum. Additionally, the low frequencies ($f^* < 0.1$) of the calculated spectra are somewhat more energetic than is the Kaimal spectrum. At the highest frequencies, our spectra become more uncertain because of instrument noise and begin to flatten out, possibly because of viscous dissipation. Nondimensional power spectra of the vertical velocity fluctuations are also presented and compared to the Kaimal curves and a −5/3 power law in Figure 3.

[16] Similar to $S^*_{u'u'}$, the observed spectra ($S^*_{w'w'}$) are highly varied across individual bursts and on average are more energetic at any given frequency than is the Kaimal spectrum. Like the horizontal velocity components, the low frequencies ($f^* < 0.1$) are more energetic than is the Kaimal spectrum. This is especially the case in the max flood events, while on the max ebb events, the lower confidence interval just captures the Kaimal spectrum.

3.2. Momentum Flux Cospectra

[17] Calculated nondimensional cospectra of the along-channel and vertical velocity fluctuations, i.e., the vertical fluxes of horizontal momentum, are plotted against the Kaimal curves for both the max flood and ebb events in Figure 4. A −7/3 power law is also plotted since the cospectra should follow a −7/3 spectral slope in the inertial subrange [*Wyngaard and Coté*, 1972; *Kaimal et al.*, 1972].

[18] The calculated cospectra follow the general shape of the Kaimal curves and −7/3 power law. Yet, as with the spectra, the calculated cospectra have higher covariance

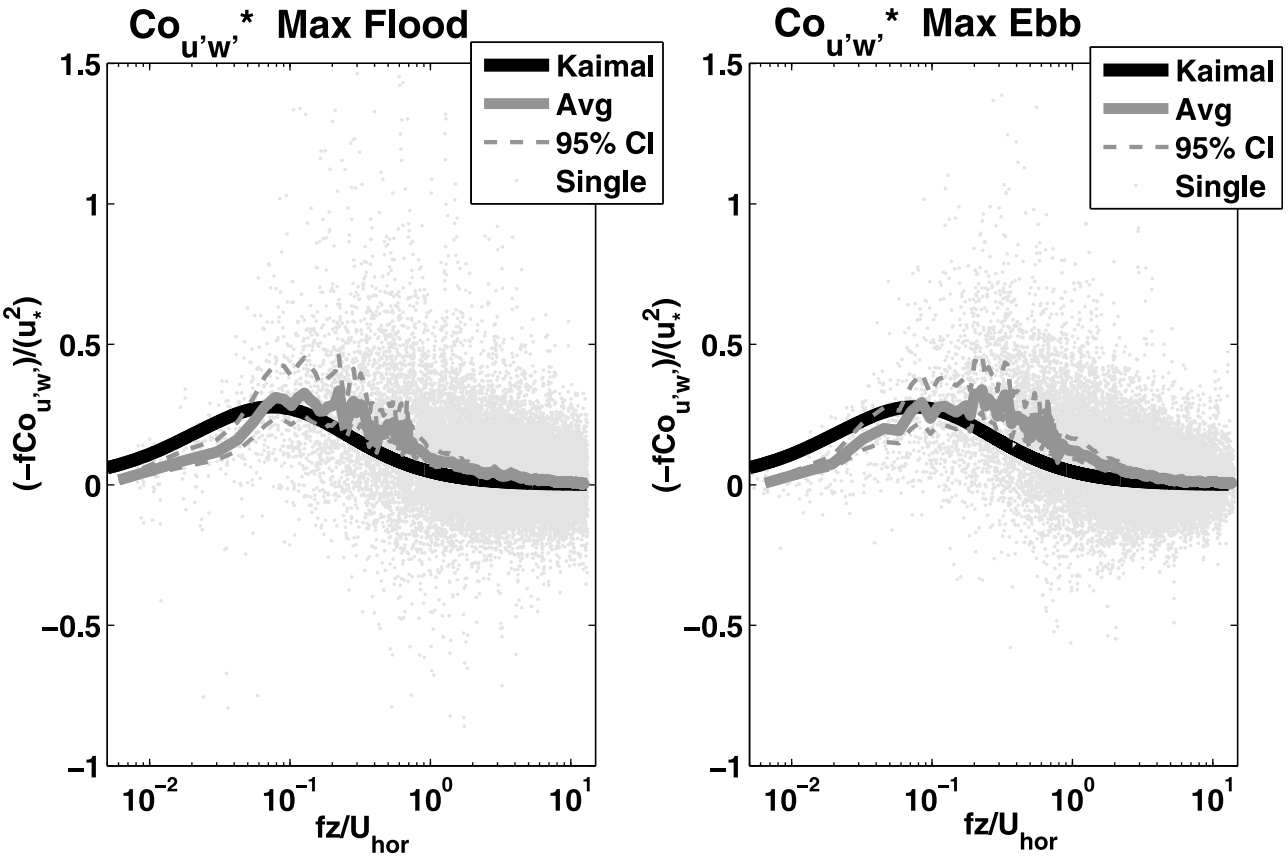

Figure 5. Nondimensional cospectra of along-channel and vertical velocity fluctuations for the max (left) flood and (right) ebb events in alternative nondimensional form and on a semilog plot. The individual cospectra are denoted by light gray dots, the frequency-averaged cospectrum by a solid dark gray line, 95% confidence intervals for the frequency-averaged cospectrum by dashed gray lines, and the *Kaimal et al.* [1972] universal curve by a solid black line.

values at any given frequency than does the Kaimal curve. However, unlike the spectra, at the low-frequency end of the cospectra ($f^* < 0.1$), the observed values fall somewhat below the Kaimal curves.

[19] In order to highlight negative covariance values, and hence countergradient momentum fluxes, an alternative nondimensional form of the cospectra is plotted in Figure 5. The cospectra are extremely erratic and highly unpredictable across individual 10 min data bursts. Frequent sign reversals are also seen across all frequencies.

3.3. Total Momentum Flux Ogive Curves

[20] Nondimensional ogive curves, which represent the cumulative flux of horizontal momentum in the vertical direction at a particular frequency, are compared to the Kaimal curves, in Figure 6. It is important to note that many individual spectra deviate significantly from the Kaimal forms, particularly at low frequencies where large countergradient fluxes are common. Indeed, at an early point in our study, an examination of data bursts from one tidal cycle showed that only approximately half of the bursts exhibited cospectra and/or ogive curves that in any way resembled the Kaimal curves.

[21] The observed ogive curves are shifted to the right of the universal curves, indicating that the largest streamwise scale motions near the bottom in our estuarine channel contribute less to the overall transfer of momentum than was observed by *Kaimal et al.* [1972] in the ABL. Given that these large eddies are thought to be important contributors to the overall momentum fluxes [*Lien and Sanford*, 2000; *Stacey et al.*, 1999], this may indicate that the overall momentum transfer from the bed to the overlying flow may be reduced relative to that which would be expected for a canonical channel flow.

3.4. Turbulent Kinetic Energy, Production, and Dissipation

[22] In canonical, homogeneous shear flows, the ratio of the principal Reynolds shear stress to the TKE is found to be a constant, i.e., $-\overline{u'w'}/k \approx 0.3$ [*Pope*, 2000]. We can examine the extent to which this behavior appears in our data by examining the spectral variation of this ratio, which is plotted for the max flood and ebb periods in Figure 7 and again compared to the canonical value.

[23] Data from both periods exhibit ratios much smaller than the canonical value of 0.3 across all frequencies, especially at higher frequencies. This indicates that the efficiency of creation of momentum fluxes by turbulence is lower than in a canonical, homogeneous shear flow, an effect seen, for example, in density stratified flows [see, e.g., *Holt et al.*, 1992]. *Scully et al.* [2011] argue that this behavior may be the result of the advection of turbulent

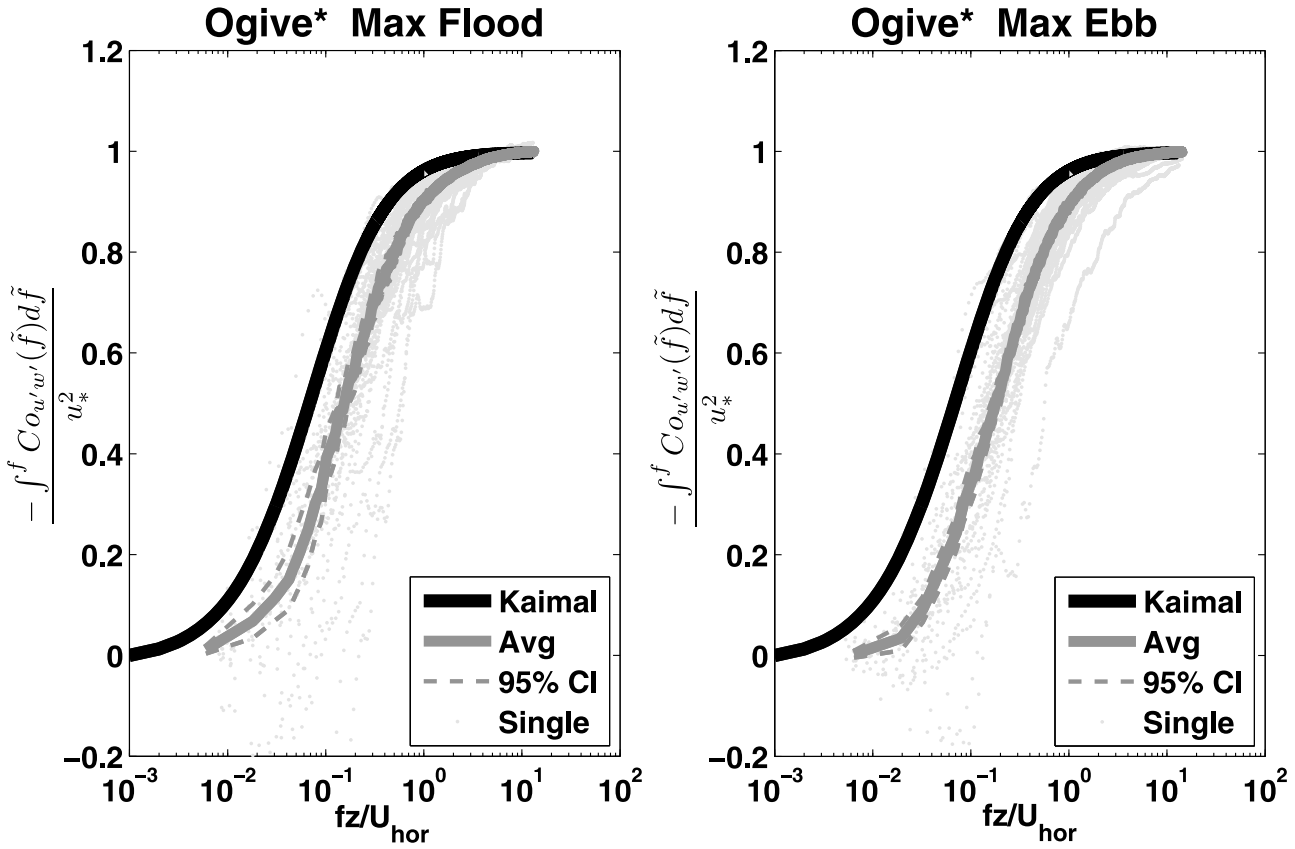

Figure 6. Nondimensional ogive curves of along-channel and vertical velocity covariances for the max (left) flood and (right) ebb events. The individual curves are denoted by light gray dots, the frequency-averaged curve by a solid dark gray line, 95% confidence intervals for the frequency-averaged curve by dashed gray lines, and the *Kaimal et al.* [1972] universal curve by a solid black line.

kinetic energy generated elsewhere, i.e., lack of a local equilibrium.

[24] An easy check of local equilibrium is to compare production and dissipation of turbulent kinetic energy with each other (Figure 8), noting that local buoyancy flux effects have been ignored because of insignificant stratification. In our case, we find that dissipation values are more than triple those of production for both periods, confirming that the turbulence we observed was not in local equilibrium. Note that the values of ε that are larger on the ebb than on the flood reflect the ebb dominance of Elkhorn Slough [*Nidzieko et al.*, 2009].

4. Discussion

4.1. Low-Frequency Behavior of Spectra

[25] Both velocity power spectra were more energetic at low frequencies than are shown by the Kaimal curves, an effect that was particularly evident in the vertical velocity spectra, especially during periods of max flood tide. This same behavior has been observed in the MBBLs [e.g., *Scully et al.*, 2011; *Soulsby*, 1977] and in many studies in the ABL over various terrains and containing inhomogeneous boundary conditions [e.g., *Al-Jiboori et al.*, 2001; *Andreas*, 1987; *Högström et al.*, 1982; *Li et al.*, 2007; *McNaughton and Laubach*, 2000; *Roth et al.*, 1989; *Smeets*

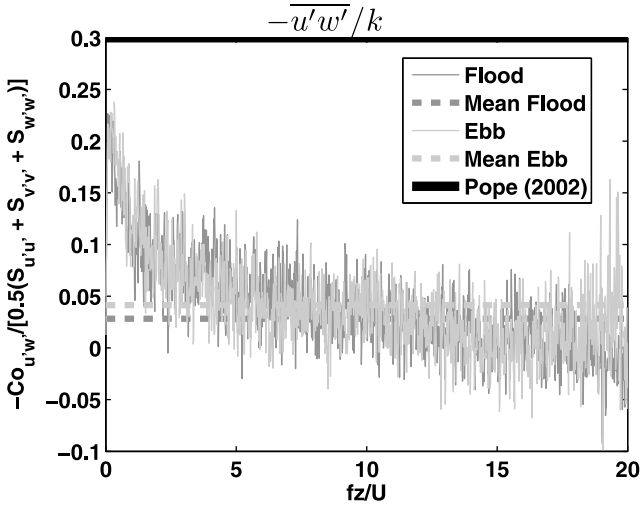

Figure 7. Spectral representation of the ratio of momentum flux to turbulent kinetic energy for both the max flood and ebb events. The canonical equilibrium turbulence value of 0.3 is indicated with a solid black line [*Pope*, 2000], the average flood event with a dark gray line, the average ebb event with a light gray line, and the mean of the frequency-averaged flood and ebb events with dashed dark and light gray lines.

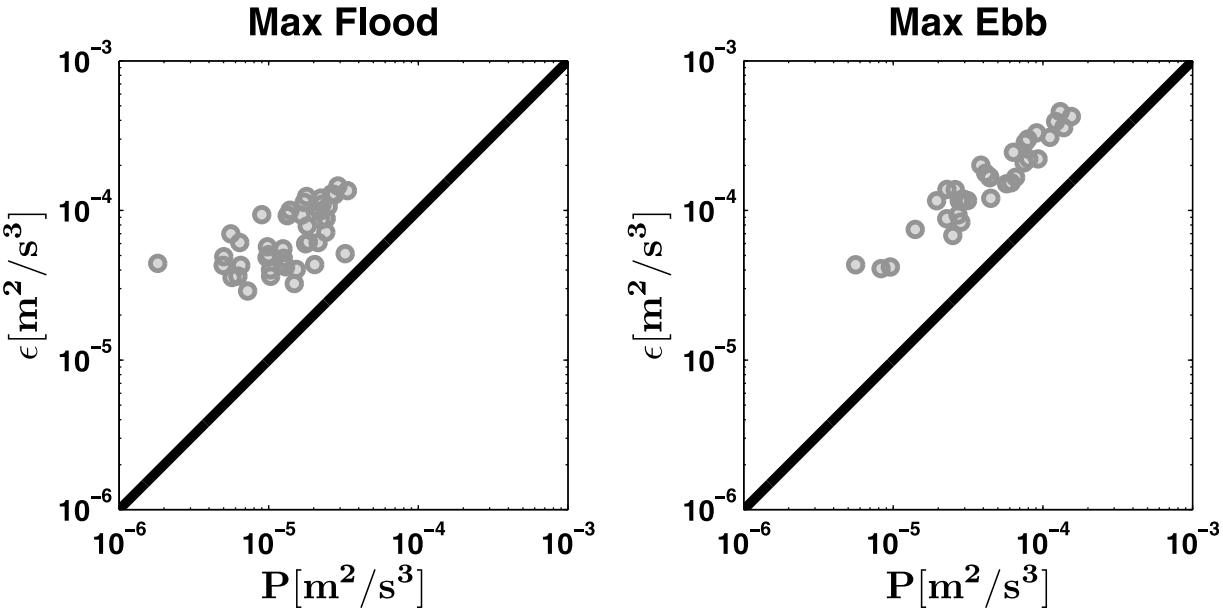

Figure 8. Production (P) and dissipation (ε) of turbulent kinetic energy for both the max (left) flood and (right) ebb events. Production was calculated using equation (8) and dissipation with equation (9). Individual events are indicated with gray circles, while the solid black line represents equilibrium turbulence ($P = \varepsilon$).

et al., 1998; *Zhang et al.*, 2010]. Taken collectively, these results suggest that something affects the large-scale turbulent structures in many natural flows.

[26] Previous studies attribute stratification and internal waves to differing energetics at low frequencies [*Lien and Sanford*, 2004; *Zhang et al.*, 2010]. Yet, in the absence of significant internal waves, stratification would act to suppress turbulence and limit the largest eddy length scales. As mentioned previously, vertical density measurements indicated approximately well-mixed conditions throughout the study period except for a small precipitation event. All calculated curves were reanalyzed, excluding the small time period of weak stratification from the precipitation, and all these curves were nearly indistinguishable from the curves over the entire study period (not shown). Hence, stratification and internal waves were likely not contributing to low-frequency deviations.

[27] Another factor affecting the turbulence we observed could have been the rough, inhomogeneous bathymetry of the study site, with nearby irregular eelgrass patches up to 2 m depth and deep scour holes (see Figure 1), typical of the bottom variability found in estuaries. One study of the ABL over rough, urban terrain found deviations from the Kaimal curves at low frequencies similar to those we observe and suggested that internal boundary layers may affect turbulent dynamics [*Högström et al.*, 1982]. These internal boundary layers may form in transitions from rough to smooth boundaries; such is the case in this study because of eelgrass patches upstream of the measurement site on both the flood and ebb periods (see Figure 1). While turbulent transfer may occur between the "inner" and "outer" boundary layers, it is more likely that internal boundary layers would constrain the largest length scales at low frequencies (much like the free surface constrains the largest length scales). This would then result in less energy at low frequencies, which is not the case in this study.

[28] On the other hand, studies in the ABL over inhomogeneous terrain suggest that spectral lag may cause more energetic values at low frequencies in rough to smooth transitions [*Al-Jiboori et al.*, 2001; *Högström et al.*, 1982; *Li et al.*, 2007; *Panofsky et al.*, 1982], a consequence of the fact that the largest (low frequencies) eddies take longer to adjust than do smaller scales (higher frequencies) in decaying turbulence [see *Batchelor*, 1953]. Hence, irregularities and increased turbulence in the bathymetry upstream of the sample site (e.g., eelgrass patches and channel shoals especially seen upstream of the flood tide; Figure 1) will locally input relatively large amounts of energy into the flow because of shear production. For example, *Lacy and Wyllie-Echeverria* [2011] found increased turbulence and friction velocities at sites containing eelgrass canopies compared with unvegetated, sandy sites. As the energy input from shear production is reduced near the measurement site and the turbulence decays, the spectra are not in equilibrium. While the small scales at high frequencies adjust rapidly to the new conditions and local momentum flux, the large scales at low frequencies lag significantly (spectral lag) and tend to preserve their shape and energy from upstream conditions. Thus, irregularities of the MBBL could have caused the observed deviations from the Kaimal curves at low frequencies.

[29] Another phenomenon that may be contributing to the low-frequency energy of the calculated curves are very long, meandering "superstructures" that have been observed in the ABL [*Hutchins and Marusic*, 2007; *Drobinski et al.*, 2004]. While the exact mechanism of formation is still unknown, the superstructures often exceed 20 times the boundary layer thickness in length, are typically smaller

than the boundary layer thickness in the spanwise direction, meander substantially along their length, possibly explaining the variability of low-frequency energy in the along-channel velocity spectra observed in this study, and are hypothesized to affect the low-frequency energy of all velocity components ($S^*_{v'}$ were also more energetic than the Kaimal curves at low frequencies in this study, but are not shown for brevity) [*Hutchins and Marusic*, 2007]. While the measurements in this study lack the temporal and spatial resolution necessary for detection of these superstructures, they may be an important mechanism affecting the turbulent dynamics at low frequencies.

4.2. Cospectra Erratic Behavior and Countergradient Momentum Fluxes

[30] The cospectra curves show the most erratic and unpredictable behavior across individual events, partially because there are both positive and negative values. These negative values, which are seen across all frequencies, might represent countergradient momentum fluxes. Likewise, the cospectra were less energetic at low frequencies relative to the Kaimal curves. Erratic variability of the cospectra and/or frequent sign reversals has been observed in the MBBL [e.g., *Gross and Nowell*, 1985; *Lien and Sanford*, 2000; *Scully et al.*, 2011; *Soulsby*, 1977] and under various conditions in the ABL [e.g., *Andreas*, 1987; *Chimonas*, 1985; *Foken*, 2008; *Gal-Chen et al.*, 1992; *Prabha et al.*, 2007; *Roth et al.*, 1989; *Sakai et al.*, 2001; *Smeets et al.*, 1988; *Zhang et al.*, 2010].

[31] While Figure 5 depicts that, on average, the momentum flux is down gradient (positive values across all frequencies for frequency-averaged curve), it is important to determine whether the countergradient fluxes (negative values) seen in individual cospectra are physical or are due to uncertainty. In order to assess the uncertainty associated with the individual cospectra in Figure 5, nondimensional standard deviations from the mean curve at a particular frequency were calculated across different frequency ranges. For low frequencies ($f^* < 10^{-1}$), the average standard deviations at a particular frequency for the flood and ebb events were 0.18 and 0.14, respectively. At intermediate frequencies ($10^{-1} < f^* < 10^{0}$), the average standard deviations from the mean at a particular frequency for flood and ebb events, respectively, were 0.23 and 0.21. Finally, at high frequencies ($f^* > 10^{0}$), the standard deviations were 0.07 for both events. Given the values above, it is conceivable that some of the countergradient fluxes may be due to uncertainties; however, given the large deviation from the mean of many of the individual events seen in Figure 5 (especially several events in the low-frequency range and many of the events at high frequencies), it is likely that many of the negative cospectral values are physical.

[32] Direct numerical simulations (DNSs) and large eddy simulations (LESs) of stratified turbulence frequently show countergradient fluxes when stratification effects are pronounced [*Holt et al.*, 1992]. Similar to the effect of stratification, it seems conceivable that in our case countergradient momentum fluxes may reflect the effects of the free surface and limited depth on the largest scales of motion. In the case of the atmospheric flow studied by *Kaimal et al.* [1972], the measurements were made close to the boundary relative to the overall depth of the planetary boundary layer. Examining $Co^*_{u'w'}$ from Figure 4, the deviation from the Kaimal curves typically occurs around $f^* = fz/U_{hor} = 10^{-1}$. Invoking Taylor's frozen turbulence hypothesis ($k_{wave} = \frac{2\pi f}{U_{hor}}$, where k_{wave} is a wave number), this corresponds to a streamwise length scale of 10 m. Given that the average depth in the estuary was 6 m during the max flood and ebb periods, the free surface may act to squash the largest eddies, thereby causing the deviation of the cospectra at low frequencies. This is supported by field observations where eddies were seen at the surface and by calculations of the average integral length scales, which were found to be around 5.4 m and 5.7 m for the flood and ebb events, respectively. The average integral length scale was found by integrating the autocorrelation function over time for each burst and converting to a length scale by invoking Taylor's frozen field turbulence hypothesis. *Gross and Nowell* [1985] observed that the largest eddies in a well-mixed tidal channel had been flattened out because of the free water surface so that the cospectra may not have been representing the low-frequency scales correctly; however, they also found that vertical velocity spectra were reduced at low frequencies, which is not the case in this study. The fact that the observed momentum flux cospectra fall significantly below the Kaimal curves at low frequencies supports the view that the limited depth is acting to alter the turbulence, but this is in contrast to what is observed with the turbulence spectra where it is expected that the limited depth would enhance the along-channel velocity spectra and diminish the vertical velocity spectra with respect to the Kaimal curves. Additionally, spectral ratios of vertical to horizontal velocity variances (not shown) depict a value just over the canonical value of 4/3 expected in the inertial subrange for isotropic turbulence and fall below this value at lower frequencies similar to what was found by *Kaimal et al.* [1972]. Thus, there is likely another mechanism besides the limited depth contributing to low-frequency deviations of the cospectra from the Kaimal curves and countergradient fluxes that is still unknown.

[33] Countergradient momentum fluxes have been ubiquitously observed in turbulent boundary layers under various conditions. Previous studies in the ABL found frequent sign reversals of the cospectra (countergradient momentum fluxes) that were due to unstable stratification and convective motions [*Andreas*, 1987; *Gerz and Shumann*, 1996; *Roth et al.*, 1989; *Sakai et al.*, 2001; *Zhang et al.*, 2010], influences of irregular topography and vortical motions [*Andreas*, 1987; *Foken*, 2008; *Smeets et al.*, 1998], and atmospheric waves [*Chimonas* 1985; *Gal-Chen et al.*, 1992]. Given that the current study took place under well-mixed conditions and that there were no significant surface waves present, these mechanisms are unlikely. The long meandering superstructures may contribute to the observed stresses [e.g., *Hutchins and Marusic*, 2007]; however, this cannot be confirmed with the measurements taken. Other mechanisms that remain to be identified are partially responsible for the erratic and highly unpredictable nature of the cospectra.

4.3. Nonequilibrium Turbulence

[34] Velocity spectra and cospectra curves were consistently shifted toward higher frequencies, indicating that observed spectral values fell above the Kaimal curves at any given frequency. Although never addressed in the respective studies, this same feature has been observed in the ocean

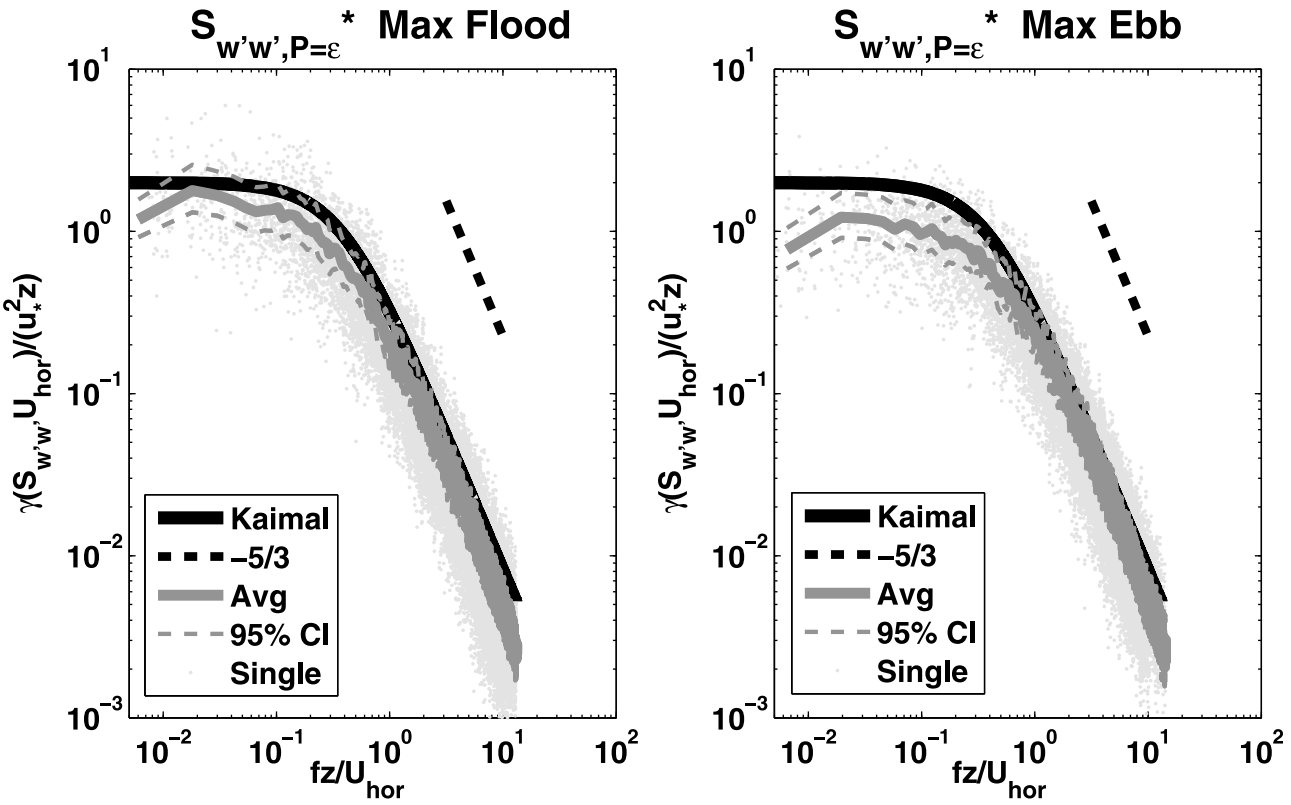

Figure 9. Nondimensional power spectra of vertical velocity fluctuations for the max (left) flood and (right) ebb events. Calculated spectra are scaled so that dissipation (ε) equals production (P) of turbulent kinetic energy in the inertial subrange. The scaled individual spectra are denoted by light gray dots, the scaled and frequency-averaged spectrum by a solid dark gray line, 95% confidence intervals for the scaled and frequency-averaged spectrum by dashed gray lines, the *Kaimal et al.* [1972] universal curve by a solid black line, and the −5/3 power law in the inertial subrange by a dashed black line.

and estuarine boundary layers [*Soulsby*, 1977; *Scully et al.*, 2011] and over urban terrain in the atmosphere [*Al-Jiboori et al.*, 2001]. Observed ratios of momentum flux to turbulent kinetic energy suggest that turbulent kinetic energy was advected into the measurement volume [*Scully et al.*, 2011; *Gross and Nowell*, 1983]. The absence of equilibrium was confirmed by our observation that dissipation rates were more than triple production rates. Since the Kaimal curves were derived on the basis of equilibrium ($P = \varepsilon$), it seems likely that the spectral shift we observe is a result of this lack of equilibrium.

[35] As seen in equation (9), spectral energy density is proportional to $\varepsilon^{2/3}$ in the inertial subrange. Thus, advection of turbulent kinetic energy into the region that causes an increase in ε will result in spectral energy densities that are larger than the equilibrium values intrinsic to the Kaimal curves. In light of this, $S^*_{u'u'}$, $S^*_{w'w'}$, and $Co^*_{u'w'}$ were all recalculated and scaled to equilibrium turbulence values by multiplying by $\gamma = (\varepsilon_{\text{equilibrium}}/\varepsilon_{\text{nonequilibrium}})^{2/3}$, where $\varepsilon_{\text{equilibrium}}$ is the equilibrium dissipation value determined from production and $\varepsilon_{\text{nonequilibrium}}$ is the nonequilibrium value of dissipation originally calculated ($\overline{\gamma} = 0.36$ and 0.43 for max flood and ebb events, respectively). Figure 9 illustrates the effect of this scaling on the power spectra of the vertical velocity fluctuations.

[36] Both the average max flood and ebb events follow the Kaimal curves much more closely in the inertial subrange. Equation (9), which was used to derive the scaling, is valid only in the inertial subrange, indicating that the effect of scaling in the low-frequency range ($f^* < 0.1$) cannot be determined and the discussion above concerning turbulence alteration is unaffected. The scaled along-channel velocity spectra and cospectra yield a similar match in the inertial subrange (not shown). This suggests that the spectral shift in the inertial subrange portion of the curves toward higher frequencies further supports the hypothesis that the turbulence we observed was not in equilibrium.

[37] A further check on our revised dissipation scaling can be had by considering the law of the wall values of turbulence dissipation $\varepsilon \approx u_*^3/(\kappa z)$, where $\kappa = 0.41$ is the von Kármán constant [*Pope*, 2000]. Figure 10 shows a plot of the dissipation against the law of the wall scaling expected in an equilibrium boundary layer flow, where the dissipation ($\varepsilon = \varepsilon_{\text{equilibrium}} + \varepsilon_{\text{excess}}$) has been decomposed into two components. The equilibrium dissipation ($\varepsilon_{\text{equilibrium}} = P$) is equal to the turbulent production calculated using equation (10), while the excess dissipation ($\varepsilon_{\text{excess}} = \varepsilon - P$) represents the remaining dissipation after subtraction of the equilibrium dissipation. While the observed dissipation rates (ε) do not match the law of the wall scaling, the equilibrium dissipation ($\varepsilon_{\text{equilibrium}}$) values follow the scaling.

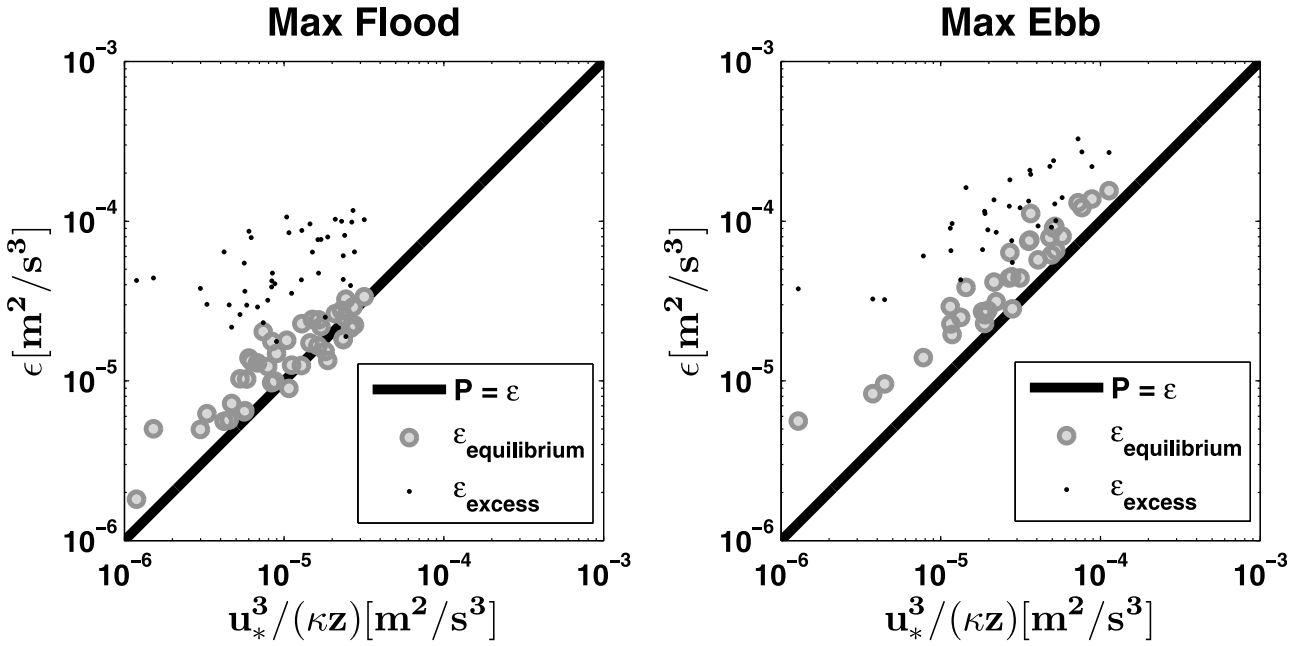

Figure 10. Dissipation (ε) of turbulent kinetic energy against the scaling of dissipation expected in an equilibrium boundary layer flow, $\varepsilon_{equilibrium} \sim u_*^3/(\kappa z)$. The solid black line represents equilibrium turbulence ($P = \varepsilon$); the gray circles are the production values calculated using equation (10), which represent the equilibrium dissipation values ($\varepsilon_{equilibrium} = P$); and the black dots represent the excess dissipation ($\varepsilon_{excess} = \varepsilon - P$) found by subtracting the production ($\varepsilon_{equilibrium} = P$) from the nonequilibrium value of dissipation (ε) originally calculated using equation (9).

[38] Likewise, the excess dissipation (ε_{excess}) was proportional to $u_*^{2.6}$ (not shown), implying that the local friction velocity is smaller than the friction velocity in the region where the excess dissipation was generated. Differences in the friction velocity can be attributed to irregularities in bathymetry and bottom roughness in the MBBL.

4.4. Total Momentum Flux Estimates

[39] The calculated ogive curves were shifted toward higher frequencies than what are seen in the Kaimal curves and often showed large regions of countergradient momentum fluxes, particularly at low frequencies. One application of the Kaimal curves is to use them to filter out wave effects on turbulent fluxes or to assess the quality of wave-turbulence separations [*Shaw and Trowbridge*, 2001; *Feddersen and Williams*, 2007; *Davis*, 2008; *Kirincich et al.*, 2010]. Often, screening criteria based on the wave orbital velocities and wavelengths will result in the elimination of many measurements. For instance, one study of the coastal ocean had to eliminate 40% of the data and stress measurements based on the initial screening criteria of the wave properties [*Kirincich et al.*, 2010]. Given that these methods rely on the comparison of the nondimensional ogive curves with respect to the Kaimal curves and that the methods already allow for limited measurements because of the presence of waves, estimates on the uncertainty of the ogive curves and total momentum flux estimates need to be addressed.

[40] In much of our data, deviation of the calculated ogive curves from the Kaimal curve was the result of countergradient momentum fluxes, as discussed in section 4.2. Table 1 displays the percentage of occurrence of these fluxes across all events in the low-frequency range. In order to quantify the countergradient fluxes and estimate deviations of the ogive curves from the Kaimal curves, the nondimensional frequency range, $df^* = f_2^* - f_1^*$, where f_1^* and f_2^* are the beginning and end frequencies of the countergradient fluxes in the low-frequency range, was calculated; the results are displayed in Table 1. Also shown is the median of the maximum negative and maximum positive values of the ogive curves that displayed countergradient fluxes at low frequencies. Taking the ratio of these two values (last row of Table 1) yields a percentage that represents an approximate assessment of the magnitude of the countergradient fluxes.

[41] Both ebbs and floods show similar ranges of countergradient fluxes in the low frequencies. While 37.8% (37.6%) of the max ebb (all ebb) events had countergradient fluxes in the low-frequency range, this resulted in only a

Table 1. Uncertainty Analysis of the Non-dimensional Ogive Curves With Respect to Counter-gradient Fluxes in the Low-Frequency Range on the Maximum Flood and Ebb Events, Respectively, Compared to All Flood and Ebb Events

Quantity	Max Flood	All Flood	Max Ebb	All Ebb
% Occurrence	27.4%	28.1%	37.8%	37.6%
Mean f_1^*	1.1E-02	2.1E-02	8.5E-03	1.8E-02
Mean f_2^*	2.9E-02	4.5E-02	2.6E-02	3.9E-02
Mean df^*	1.8E-02	2.4E-02	1.7E-02	2.1E-02
Median Min Ogive*	−0.11	−0.08	−0.04	−0.05
Median Max Ogive*	1.00	1.00	0.99	1.00
Median |Min/Max| %, Ogive*	11.3%	8.3%	4.0%	5.0%

4.0% (5.0%) change in the normalized amplitude. On the other hand, 27.4% (28.1%) of the max flood (all flood) events resulted in a normalized amplitude change of 11.3% (8.3%). There was little difference between the max flood and ebb events and all flood and ebb events, indicating that deviations in the ogive curves that were due to countergradient fluxes occur independently of flow strength. Another study [*Feddersen and Williams*, 2007] rejected Reynolds stress estimates based on heuristically selected limits to the ogive curves and found between 23% and 35% of events failed the ogive curve test using one method [*Feddersen and Williams*, 2007] and between 40% and 60% using another method [*Shaw and Trowbridge*, 2001]. While removing some of the uncertainties of the individual curves by averaging over longer time periods and/or shorter windowed segments may improve agreement of individual curves to the Kaimal curves, there are still countergradient fluxes that are due to physical phenomena as well as uncertainties from nonequilibrium turbulence that are due to inhomogeneous streamwise turbulence. Hence, the frequency of occurrence of these large countergradient fluxes and deviations of the ogive curves from the Kaimal curves may need to be taken into account when considering using ogive curves to estimate momentum fluxes and removing wave effects from turbulent flux signals.

5. Conclusions

[42] Turbulence power spectra, cospectra, and ogive curves calculated from ADV data taken in a shallow estuarine tidal flow were scaled according to Monin-Obukhov similarity theory to determine whether universal curves derived from a uniform, neutrally stable ABL are applicable in this case. All of the calculated curves followed the general shape of the Kaimal curves and turbulent power laws; however, the curves were all shifted toward higher frequencies. Spectral ratios of momentum flux to turbulent kinetic energy suggested that nonequilibrium turbulence was present, likely the effect of advection from upstream. Analysis of the production and dissipation of turbulent kinetic energy confirmed the presence of nonequilibrium turbulence with dissipation always exceeding production. This may have been the result of inhomogeneous bathymetry and bottom roughness. Scaling the spectra and cospectra so that the energy was equal to that expected for equilibrium conditions resulted in the curves matching up much closer to the Kaimal curves in the inertial subrange.

[43] Additionally, the along-channel and vertical velocity spectra were more energetic than the Kaimal curves at low frequencies ($f^* < 0.1$). This was likely due to rougher conditions upstream of the measurement site and the phenomenon of spectral lag in decaying turbulence, whereby the largest eddies (low frequencies) take longer to adjust to changes in bottom conditions. Internal boundary layers and long meandering "superstructures" may have also contributed to the low-frequency deviations. Additionally, momentum flux cospectra underestimated stresses at low frequencies ($f^* < 0.1$). Consideration of the turbulence length scales involved suggests that the largest eddy length scales might have been altered by the presence of the water surface or, equivalently, the limited depth. This suggests that the results from *Kaimal et al.* [1972] may be directly applicable only when the measurement height is much less than the depth of the flow or thickness of the boundary layer. Likewise, the underestimation of the cospectra at low frequencies resulted in the ogive curves being shifted toward higher frequencies compared with the Kaimal curves. This produced lower estimates of total momentum fluxes than with the Kaimal curves. Calculated cospectra were also extremely variable and highly erratic, with countergradient momentum fluxes seen across all frequencies. These countergradient momentum fluxes, especially at low frequencies, resulted in uncertainties in the ogive curves, which have implications for methods that use ogive curves for the removal of wave effects from turbulent flux signals

[44] One consequence of our results is that it shows that there are limits to the applicability of ABL similarity scaling to ocean and estuarine flows. While the general shapes and slopes of the universal curves match our data, spectral energy densities and momentum fluxes were different, possibly reflecting the behavior of nonequilibrium turbulence that might characterize the irregular and inhomogeneous bottom boundary layers likely to be found in the ocean and in estuaries. Finally, use of the Kaimal curves to remove waves from turbulent signals should be done with care, given the significant deviations from those curves that are possible.

[45] **Acknowledgments.** The data were collected with support from NSF grant ECCS-0308070 to SGM as part of the LOBO program (Ken Johnson, P.I.). The analysis presented here was supported by the Department of Defense (DoD) through the National Defense Science and Engineering Graduate Fellowship (NDSEG) Program and through ONR grant N00014-10-1-0236 (Scientific officers: Thomas Drake, C. Linwood Vincent, and Terri Paluszkiewicz). Additional support was provided by the Stanford Graduate Fellowship (SGF). Special thanks to Derek Fong and Jim Hench for the original data collection and experimental design.

References

Al-Jiboori, M. H., Y. Xu, and Y. Qian (2001), Velocity spectra over different terrains, *Atmos. Sci. Lett.*, *2*, 32–38, doi:10.1006/asle.2001.0042.

Andreas, E. L. (1987), Spectral measurements in a disturbed boundary layer over snow, *J. Atmos. Sci.*, *44*, 1912–1939, doi:10.1175/1520-0469(1987)044<1912:SMIADB>2.0.CO;2.

Batchelor, G. K. (1953), *The Theory of Homogeneous Turbulence*, Cambridge Univ. Press, New York.

Chimonas, G. (1985), Apparent counter-gradient heat fluxes generated by atmospheric waves, *Boundary Layer Meteorol.*, *31*, 1–12, doi:10.1007/BF00120030.

Davis, K. A. (2008), Dynamics of internal waves on the southeastern Florida Shelf: Implications for cross-shelf exchange and turbulent mixing on a barrier reef system, Ph.D. dissertation, Dept. of Civil and Environ. Eng., Stanford Univ., Stanford, Calif.

Drobinski, P., P. Carlotti, R. K. Newsom, R. M. Banta, R. C. Foster, and J. Redelsperger (2004), The structure of the near-neutral atmospheric surface layer, *J. Atmos. Sci.*, *61*, 699–714, doi:10.1175/1520-0469(2004)061<0699:TSOTNA>2.0.CO;2.

Emery, W. J., and R. E. Thomson (2004), *Data Analysis Methods in Physical Oceanography*, 2nd ed., 638 pp., Elsevier, Amsterdam.

Feddersen, F., and A. J. Williams (2007), Direct estimation of the Reynolds stress vertical structure in the nearshore, *J. Atmos. Oceanic Technol.*, *24*, 102–116, doi:10.1175/JTECH1953.1.

Foken, T. (2008), The energy balance closure problem: An overview, *Ecol. Appl.*, *18*, 1351–1367, doi:10.1890/06-0922.1.

Gal-Chen, T., M. Xu, and W. L. Eberhard (1992), Estimations of atmospheric boundary layer fluxes and other turbulence parameters from Doppler lidar data, *J. Geophys. Res.*, *97*, 18,409–18,423, doi:10.1029/91JD03174.

Gerz, T., and U. Schumann (1996), A possible explanation of countergradient fluxes in homogeneous turbulence, *Theor. Comput. Fluid Dyn.*, *8*, 169–181, doi:10.1007/BF00418056.

Gross, T. F., and A. R. M. Nowell (1983), Mean flow and turbulence scaling in a tidal boundary layer, *Cont. Shelf Res.*, *2*, 109–126, doi:10.1016/0278-4343(83)90011-0.

Gross, T. F., and A. R. Nowell (1985), Spectral scaling in a tidal boundary layer, *J. Phys. Oceanogr.*, *15*, 496–508, doi:10.1175/1520-0485(1985)015<0496:SSIATB>2.0.CO;2.

Haugen, D. A., J. C. Kaimal, and E. F. Bradley (1971), An experimental study of Reynolds stress and heat flux in the atmospheric surface layer, *Q. J. R. Meteorol. Soc.*, *97*, 168–180, doi:10.1002/qj.49709741204.

Högström, U., H. Bergström, and H. Alexandersson (1982), Turbulence characteristics in a near neutrally stratified urban atmosphere, *Boundary Layer Meteorol.*, *23*, 449–472, doi:10.1007/BF00116272.

Holt, S. E., J. R. Koseff, and J. H. Ferziger (1992), A numerical study of the evolution and structure of homogeneous stably stratified sheared turbulence, *J. Fluid Mech.*, *237*, 499–539, doi:10.1017/S0022112092003513.

Hutchins, N., and I. Marusic (2007), Evidence of very long meandering features in the logarithmic region of turbulent boundary layers, *J. Fluid Mech.*, *579*, 1–28, doi:10.1017/S0022112006003946.

Kaimal, J. C., J. C. Wyngaard, Y. Izumi, and O. R. Coté (1972), Spectral characteristics of surface-layer turbulence, *Q. J. R. Meteorol. Soc.*, *98*, 563–589, doi:10.1002/qj.49709841707.

Kirincich, A. R., S. J. Lentz, and G. P. Gerbi (2010), Calculating Reynolds stresses from ADCP measurements in the presence of surface gravity waves using the cospectra-fit method, *J. Atmos. Oceanic Technol.*, *27*, 889–907, doi:10.1175/2009JTECHO682.1.

Kristensen, L., and D. R. Fitzjarrald (1984), The effect of line averaging on scalar flux measurements with a sonic anemometer near the surface, *J. Atmos. Oceanic Technol.*, *1*, 138–146, doi:10.1175/1520-0426(1984)001<0138:TEOLAO>2.0.CO;2.

Lacy, J. R., and S. Wyllie-Echeverria (2011), The influence of current speed and vegetation density on flow structure in two macrotidal eelgrass canopies, *Limnol. Oceanogr. Fluids Environ.*, *1*, 38–55, doi:10.1215/21573698-1152489.

Li, W., T. Hiyama, and N. Kobayashi (2007), Turbulence spectra in the near-neutral surface layer over the Loess Plateau in China, *Boundary Layer Meteorol.*, *124*, 449–463, doi:10.1007/s10546-007-9180-y.

Lien, R., and T. B. Sanford (2000), Spectral characteristics of velocity and vorticity fluxes in an unstratified turbulent boundary layer, *J. Geophys. Res.*, *105*, 8659–8672, doi:10.1029/2000JC900031.

Lien, R., and T. B. Sanford (2004), Turbulence spectra and local similarity scaling in a strongly stratified oceanic bottom boundary layer, *Cont. Shelf Res.*, *24*, 375–392, doi:10.1016/j.csr.2003.10.007.

McNaughton, K. G., and J. Laubach (2000), Power spectra and cospectra for wind and scalars in a disturbed surface layer at the base of an advective inversion, *Boundary Layer Meteorol.*, *96*, 143–185, doi:10.1023/A:1002477120507.

Nidzieko, N. J., D. A. Fong, and J. L. Hench (2006), Comparison of Reynolds stress estimates derived from standard and fast-ping ADCPs, *J. Atmos. Oceanic Technol.*, *23*, 854–861, doi:10.1175/JTECH1885.1.

Nidzieko, N. J., J. L. Hench, and S. G. Monismith (2009), Lateral circulation in well-mixed and stratified estuarine flows with curvature, *J. Phys. Oceanogr.*, *39*, 831–851, doi:10.1175/2008JPO4017.1.

Panofsky, H. A., D. Larko, R. Lipschutz, G. Stone, E. F. Bradley, A. J. Bowen, and J. Højstrup (1982), Spectra of velocity components over complex terrain, *Q. J. R. Meteorol. Soc.*, *108*, 215–230, doi:10.1002/qj.49710845513.

Perlin, A., J. N. Moum, J. M. Klymak, M. D. Levine, T. Boyd, and P. M. Kosro (2005), A modified law-of-the-wall applied to oceanic bottom boundary layers, *J. Geophys. Res.*, *110*, C10S10, doi:10.1029/2004JC002310.

Pope, S. B. (2000), *Turbulent Flows*, 771 pp., Cambridge Univ. Press, Cambridge, U. K.

Prabha, T. V., M. Y. Leclerc, A. Karipot, and D. Y. Hollinger (2007), Low-frequency effects on eddy covariance fluxes under the influence of a low-level jet, *J. Appl. Meteorol. Climatol.*, *46*, 338–352, doi:10.1175/JAM2461.1.

Roth, M., T. R. Oke, and D. G. Steyn (1989), Velocity and temperature spectra and cospectra in an unstable suburban atmosphere, *Boundary Layer Meteorol.*, *47*, 309–320, doi:10.1007/BF00122336.

Sakai, R. K., D. R. Fitzjarrald, and K. E. Moore (2001), Importance of low-frequency contributions to eddy fluxes observed over rough surfaces, *J. Appl. Meteorol.*, *40*, 2178–2192, doi:10.1175/1520-0450(2001)040<2178:IOLFCT>2.0.CO;2.

Sanford, T. B., and R. Lien (1999), Turbulent properties in a homogeneous tidal bottom boundary layer, *J. Geophys. Res.*, *104*, 1245–1257, doi:10.1029/1998JC900068.

Scully, M. E., W. R. Geyer, and J. H. Trowbridge (2011), The influence of stratification and nonlocal turbulent production on estuarine turbulence: An assessment of turbulence closure with field observations, *J. Phys. Oceanogr.*, *41*, 166–185, doi:10.1175/2010JPO4470.1.

Shaw, W. J., and J. H. Trowbridge (2001), The direct estimation of near-bottom turbulent fluxes in the presence of energetic wave motions, *J. Atmos. Oceanic Technol.*, *18*, 1540–1557, doi:10.1175/1520-0426(2001)018<1540:TDEONB>2.0.CO;2.

Shaw, W. J., J. H. Trowbridge, and A. J. Williams III (2001), Budgets of turbulent kinetic energy and scalar variance in the continental shelf bottom boundary layer, *J. Geophys. Res.*, *106*, 9551–9564, doi:10.1029/2000JC000240.

Smeets, C. J. P. P., P. G. Duynkerke, and H. F. Vugts (1998), Turbulence characteristics of the stable boundary layer over a mid-latitude glacier. Part I: A combination of katabatic and large-scale forcing, *Boundary Layer Meteorol.*, *87*, 117–145, doi:10.1023/A:1000860406093.

Soulsby, R. L. (1977), Similarity scaling of turbulence spectra in marine and atmospheric boundary layers, *J. Phys. Oceanogr.*, *7*, 934–937, doi:10.1175/1520-0485(1977)007<0934:SSOTSI>2.0.CO;2.

Soulsby, R. L. (1980), Selecting record length and digitization rate for near-bed turbulence measurements, *J. Phys. Oceanogr.*, *10*, 208–219, doi:10.1175/1520-0485(1980)010<0208:SRLADR>2.0.CO;2.

Stacey, M. T., S. G. Monismith, and J. R. Burau (1999), Measurements of Reynolds stress profiles in unstratified tidal flow, *J. Geophys. Res.*, *104*, 10,933–10,949, doi:10.1029/1998JC900095.

Trowbridge, J., and S. Elgar (2003), Spatial scales of stress-carrying nearshore turbulence, *J. Phys. Oceanogr.*, *33*, 1122–1128, doi:10.1175/1520-0485(2003)033<1122:SSOSNT>2.0.CO;2.

Voulgaris, G., and J. H. Trowbridge (1998), Evaluation of the acoustic Doppler velocimeter (ADV) for turbulence measurements, *J. Atmos. Oceanic Technol.*, *15*, 272–289, doi:10.1175/1520-0426(1998)015<0272:EOTADV>2.0.CO;2.

Wyngaard, J. C., and O. R. Coté (1972), Cospectral similarity in the atmospheric surface layer, *Q. J. R. Meteorol. Soc.*, *98*, 590–603, doi:10.1002/qj.49709841708.

Zhang, Y., H. Liu, T. Foken, Q. L. Williams, S. Liu, M. Mauder, and C. Liebethal (2010), Turbulence spectra and cospectra under the influence of large eddies in the Energy Balance EXperiment (EBEX), *Boundary Layer Meteorol.*, *136*, 235–251, doi:10.1007/s10546-010-9504-1.

S. G. Monismith, Environmental Fluid Mechanics Laboratory, Stanford University, 473 Via Ortega, Room 313b, MC 4020, Stanford, CA 94305, USA. (monismith@stanford.edu)

N. J. Nidzieko, Horn Point Laboratory, University of Maryland Center for Environmental Science, 2020 Horns Point Rd., Cambridge, MD 21613, USA. (nidzieko@umces.edu)

R. K. Walter, Environmental Fluid Mechanics Laboratory, Stanford University, 473 Via Ortega, Room M-15, MC 4020, Stanford, CA 94305, USA. (rwalter@stanford.edu)